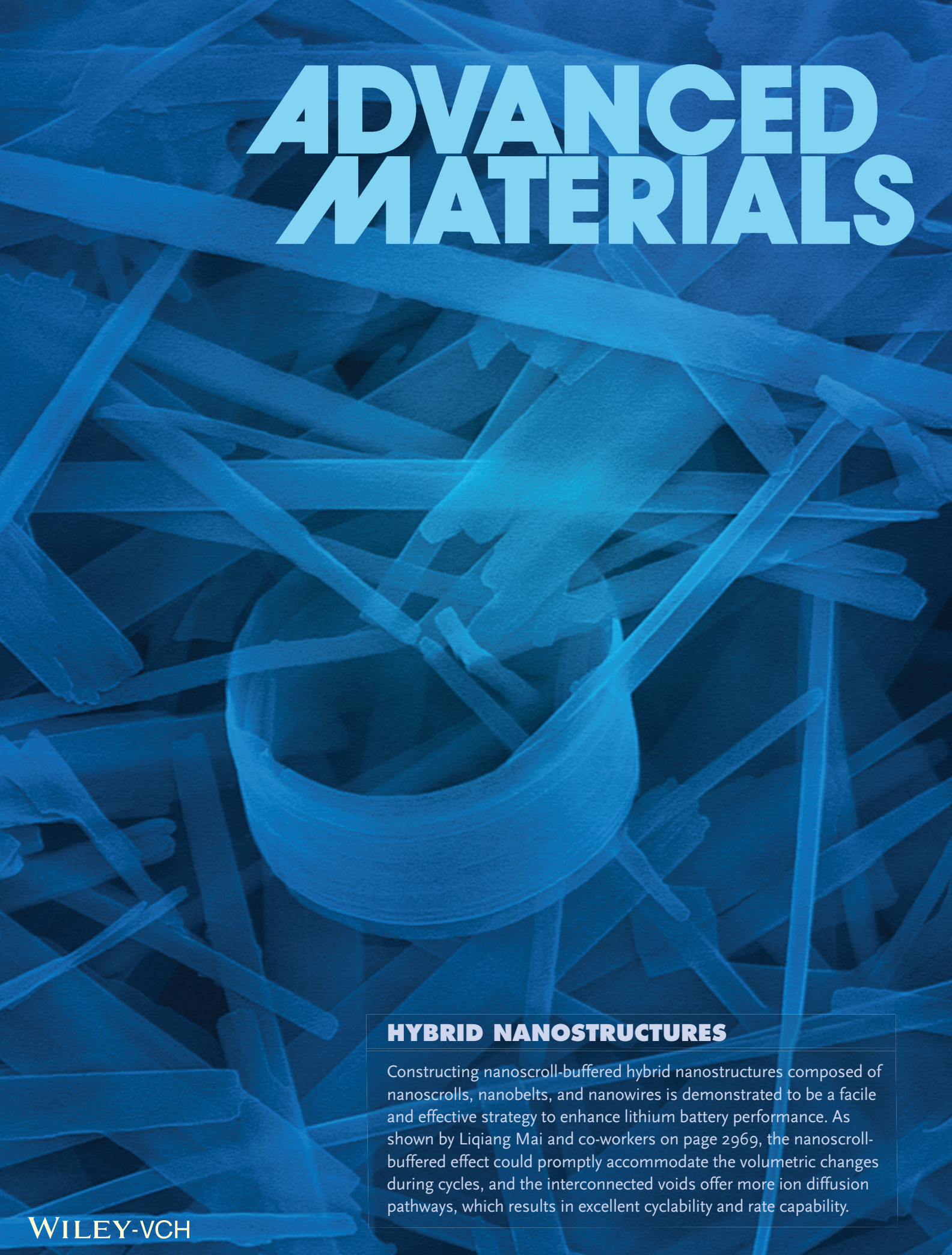


ADVANCED MATERIALS



HYBRID NANOSTRUCTURES

Constructing nanoscroll-buffered hybrid nanostructures composed of nanoscrolls, nanobelts, and nanowires is demonstrated to be a facile and effective strategy to enhance lithium battery performance. As shown by Liqiang Mai and co-workers on page 2969, the nanoscroll-buffered effect could promptly accommodate the volumetric changes during cycles, and the interconnected voids offer more ion diffusion pathways, which results in excellent cyclability and rate capability.

Nanoscroll Buffered Hybrid Nanostructural VO₂ (B) Cathodes for High-Rate and Long-Life Lithium Storage

Liqiang Mai,* Qiulong Wei, Qinyou An, Xiacong Tian, Yunlong Zhao, Xu Xu, Lin Xu, Liang Chang, and Qingjie Zhang

Rechargeable lithium batteries have been widely used for consumer electronics and are desirable for the development of hybrid electric vehicles (HEV) and electric vehicles (EV), due to their high energy density and good environment compatibility.^[1–5] Vanadium oxides with high capacity, low cost and abundant sources have been extensively investigated as potential cathode materials for next-generation lithium batteries.^[6–10] Among them, vanadium dioxide (B), denoted as VO₂ (B), is one of the most attractive electrode materials owing to its double layers of V₄O₁₀ type with tunnels for rapid lithium ion insertion/deinsertion (Figure S1) for both organic and aqueous lithium ion batteries.^[11–13] However, as a metastable phase, VO₂ (B) can be transformed to VO₂ (M) or VO₂ (R) under heat treatment or in solution reaction.^[14–16] Some reported VO₂ (B) materials showed nearly featureless discharge curves or just a hint of plateau at 2.5 V, associated with their poor crystallinity.^[10] Therefore, it is of great importance to synthesize high-crystalline and pure-phase VO₂ (B) electrode materials with excellent electrochemical performance.

The enhanced electrochemical performance of electrodes depends on not only the material intrinsic characteristics, but also the designed morphologies. For synthesized VO₂ (B) nanorods^[17], nanowires^[18] and nanobelts,^[19] their one-dimensional (1D) nanostructures can offer large surface area and efficient electron transport pathway to achieving high capacity. But these materials still suffer from fast capacity fading and poor high-rate performance, due to their aggregation and the increased charge transfer resistance during cycles.^[16–19] To improve the cyclability and rate performance, functional nanostructural architectures assembled from nanowires, nanobelts or other nanocrystals have been designed, e.g., hierarchical heterostructures,^[20] core/shell structures,^[21] mesoporous^[22] and others.^[4,16,23–25] As a functional nanostructure, nanoscroll with open ends/edges could provide easy radial expansion by interlayer sliding to buffer the swelling during lithiation/delithiation.^[26,27] Zeng et al.^[28] reported graphene scrolls with 96.8% capacity retention after 1,000 cycles, and with 50%

capacity increase compared with graphene sheets, exhibiting high flexibility and excellent structural stability. Thus, the synergistic combination of nanoscrolls with structural stability and 1D nanomaterials with efficient electron transport pathway, in homogeneous metal oxide materials, may result in the enhancement of the electrochemical performance. However, it is rarely reported and remains largely unexplored.

Here, we report a nanoscroll buffered hybrid nanostructural VO₂ (B) (HNS) composed of nanobelts and nanowires with greatly improved cycle life and rate capability. It is found that this unique HNS with buffered section provides facile strain relaxation to accommodate the volume variations during lithiation/delithiation, which may greatly enhance the structural stability and cyclability (Figure 1). Further, the interior of nanoscrolls and the interconnected voids between the hybrid nanostructures could shorten the lithium ion diffusion pathway for fast charge/discharge.^[4,5]

The crystal structure of the products is determined by X-ray diffraction (XRD) (Figure 2a). Firstly, V₃O₇·H₂O nanowires were synthesized only with polyvinyl pyrrolidone (PVP) (Figure S2). With the addition of polyethylene glycol (PEG), the peaks at 14.4, 29.0 and 44.1° appear, corresponding to the characteristic of (00 l) reflection peaks for VO₂ (B). Then, HNS was obtained with both PVP and PEG (Figure 2a,iv). As a control experiment, pure nanobelt VO₂ (B) (PNB) was synthesized with PEG (Figure 2a,v). All the diffraction peaks are indexed to the monoclinic VO₂ (B) phase (space group: C2/m) with lattice constants $a = 12.093 \text{ \AA}$, $b = 3.702 \text{ \AA}$, $c = 6.433 \text{ \AA}$ and $\beta = 106.6^\circ$ (JCPDS 81-2392). The HNS composed of nanoscrolls, nanobelts and nanowires is clearly observed in the field-emission scanning electron microscopic (FESEM) image (Figure 2b), while the PNB is only composed of nanobelts (Figure 2c). The as-synthesized HNS product exhibits a “jelly-like” shape in the optical image (Figure 2b, upper inset), while the PNB product precipitated at the beaker bottom (Figure 2c, upper inset). The high-resolution transmission electron microscopic (HRTEM) images were taken from the edge of nanobelts (Figure 2d,e, inset). The lattice fringes are clearly visible with spacing of 2.05 and 2.01 Å, which are in agreement with those of the (003) and (-601) planes of VO₂ (B). Moreover, the Brunauer-Emmet-Teller (BET) surface areas of HNS and PNB are 23.2 and 18.6 m² g⁻¹, respectively.

A probable schematic illustration of the HNS formation process is shown in Figure 2f. The V₂O₅ sols are mixed with PVP and PEG to form a homogeneous precursor. During the hydrothermal treatment, the sols are assembled to large sheets (Figure S3a). Then, some ultrathin nanoribbons are torn from the surface of the sheets and self-roll into nanoscrolls

Prof. L. Q. Mai, Mr. Q. L. Wei, Q. Y. An, X. C. Tian, Y. L. Zhao, X. Xu, L. Xu, Ms. L. Chang, Prof. Q. J. Zhang
State Key Laboratory of Advanced Technology
for Materials Synthesis and Processing
WUT-Harvard Joint Nano Key Laboratory
Wuhan University of Technology
Wuhan, 430070 P.R. China
E-mail: mlq518@whut.edu.cn



DOI: 10.1002/adma.201205185

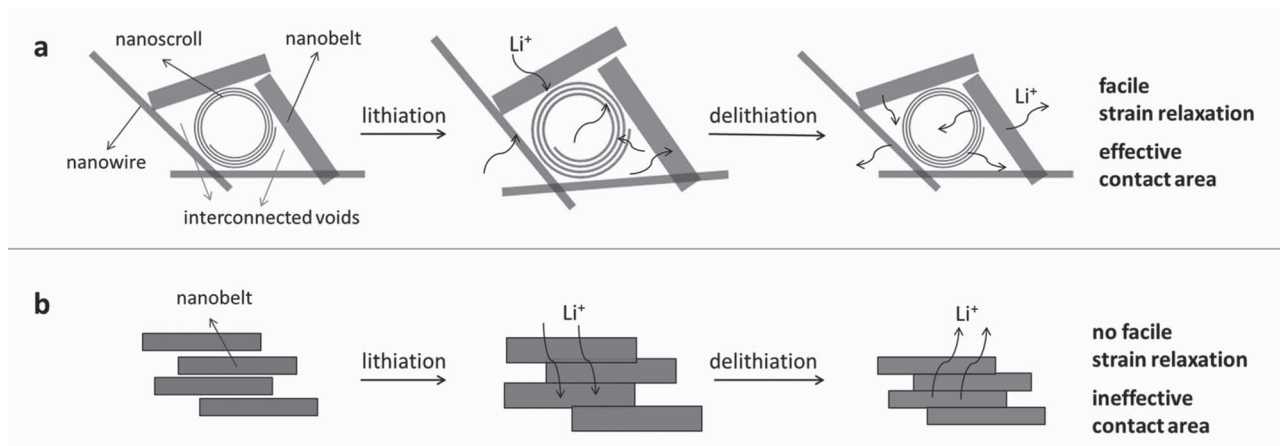


Figure 1. a) The hybrid nanostructure provides facile strain relaxation for swelling during lithiation/delithiation, and effective electrode-electrolyte contact area to shorten the ion diffusion pathway. b) In pure nanobelt structure, the strain could not completely and promptly release, and the nanobelts tend to aggregate during cycles, leading to poor cycling performance.

(Figure S3b,c). Finally, the rest of sheets are possibly split into nanobelts and nanowires. These three continuous steps result in the formation of HNS, while the PNB is obtained in one step (Figure S4). The products at different reaction time were further characterized by XRD (Figure S5), which indicated two different reduction processes to form HNS and PNB. For HNS, V_2O_5 is reduced into $V_3O_7 \cdot H_2O$ and then VO_2 (B). While for PNB, V_2O_5 is directly reduced into VO_2 (B). Here, PVP and PEG play dual roles as both reductant and surfactant to synthesize the HNS. The reducibility of PVP is attributed to the presence

of hydroxyl groups at the ends of its molecules.^[29] Similarly, the reducibility of PEG is due to its hydroxyl groups.^[30] As surfactants, PVP and PEG can be adsorbed on the surface of metal oxides and act as hydrogen-bonding acceptors in the abundant carbonyl and hydroxy systems.^[31] During the redox reaction, the changes of chemical and hydrogen bonds and the reorganization of vanadium atoms may cause the structural stress release from the surface of vanadium oxide sheets, leading to the cleavage.^[29–31] Moreover, the flexible nanoribbons roll into nanoscrolls through organic molecule self-assembly under the

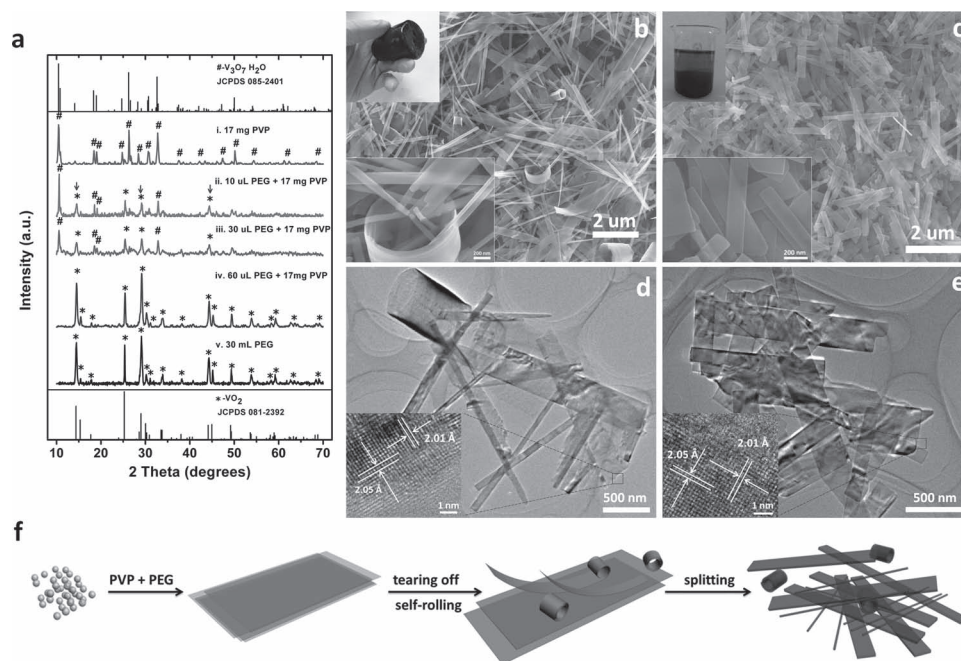


Figure 2. a) XRD patterns of the products synthesized with different amount of PEG and PVP. b,c) SEM images of the (b) hybrid nanostructural VO_2 (B) and (c) pure nanobelt VO_2 (B), respectively; the upper insets show the camera images of “jelly-like” shape and precipitated products. d,e) TEM images of the (d) hybrid nanostructural VO_2 (B) and (e) pure nanobelt VO_2 (B), respectively; the insets shows HRTEM images of the edge of nanobelts. f) Illustration of the formation of hybrid nanostructural VO_2 (B).

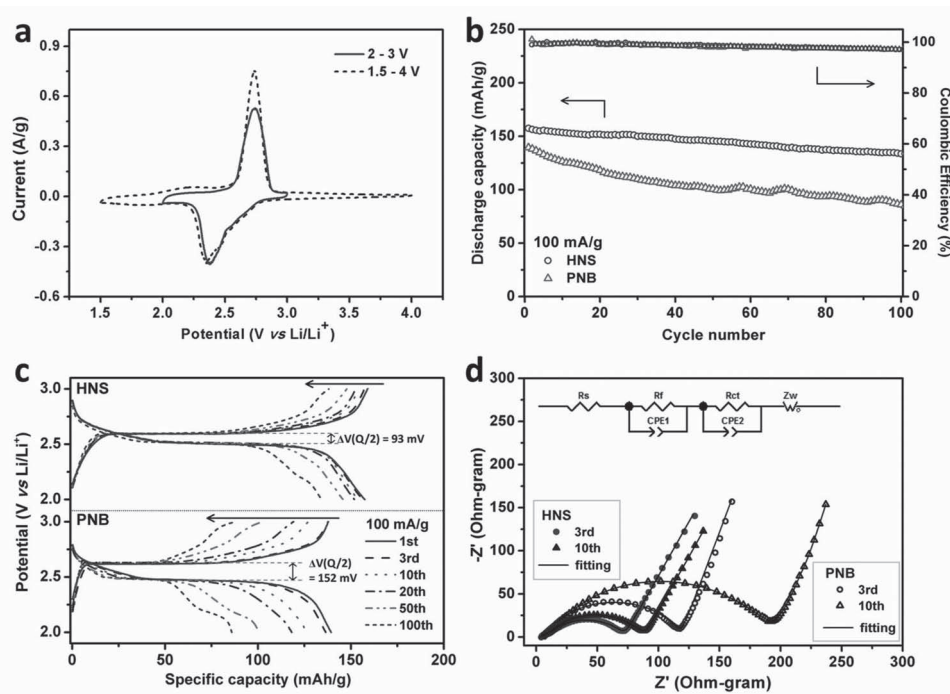


Figure 3. Electrochemical measurements of the hybrid nanostructural (HNS) and pure nanobelt (PNB) VO_2 (B) cathodes. a) Cyclic voltammograms at a scan rate of 0.2 mV s^{-1} . b) Cycling performance of the HNS and PNB cathodes cycled at 100 mA g^{-1} in 2-3 V, and the corresponding coulombic efficiency. c) Charge–discharge curves of HNS (top) and PNB (bottom) at different cycles. d) AC impedance plots of HNS and PNB cathodes, from 0.01 Hz to 100 kHz.

hydrothermal condition.^[32] Besides, the products with other proportions were further synthesized (Figure 2a, Figure S2 and Figure S6). Their morphologies tend to form nanobelts with increased amount of PEG or PVP, which are consistent with formation of PNB products. Based on the above results, the coordinated use of suitable amount of PEG and PVP is critical to synthesize the hybrid nanostructure.

Coin cells with metallic lithium as anode were assembled to investigate the electrochemical performance of the HNS and PNB cathodes. Firstly, the electrochemical properties of the cathodes were evaluated by cyclic voltammetry (Figure 3a). A pair of redox peaks occur when being tested in 2-3 V and 1.5-4 V, corresponding to the following phase transition (Equation 1):



When cycled in 1.5-4 V and at 100 mA g^{-1} (Figure S7), the initial discharge capacity of HNS cathode is 248 mAh g^{-1} , higher than that of PNB (187 mAh g^{-1}), hollow microsphere $\text{VO}_2(\text{B})$ ^[16] (195 mAh g^{-1} at 50 mA g^{-1}) and $\text{VO}_2(\text{B})/\text{C}$ nanobelts^[19] (219 mAh g^{-1} at 50 mA g^{-1}). Besides, the HNS cathode exhibits a capacity loss of 6% after 10 cycles, much lower than that of 30% for PNB, and the reported $\text{VO}_2(\text{B})$ cathodes,^[12,16–19] indicating excellent structural stability of HNS. However, after long-term cycles, an extra plateau occurs above 3 V in the charge state (Figure S7b), which leads to the coulombic efficiency decrease and capacity fading. The deep lithium ion insertion/deinsertion may cause the layered structure disorder/destruction and then capacity fading.^[6,10] In our previous

work,^[23] we reported that the ultralong hierarchical V_2O_5 nanowires cycled in 2-4 V exhibited better stability compared to the results obtained in 1.75-4 V, because the irreversible formation of $\omega\text{-Li}_3\text{V}_2\text{O}_5$ at $\sim 1.9 \text{ V}$ was avoided. Herein, based on the CV results and in order to avoid the side reaction above 3 V, a suitable potential window of 2-3 V was chosen to obtain better cyclability.

Figure 3b shows the discharge capacity of HNS and PNB cathodes in 2-3 V and at 100 mA g^{-1} ($\sim 0.7\text{C}$, a rate of 1 C corresponds to complete charge or discharge in one hour). The initial discharge capacity of HNS cathode is up to 158 mAh g^{-1} , extremely close to the theoretical capacity (161 mAh g^{-1} , $x = 0.5$ in $\text{Li}_x\text{VO}_2(\text{B})$), while the capacity of PNB cathode is 139 mAh g^{-1} . After 100 cycles, the capacities of HNS and PNB cathodes decrease to 134 and 86 mAh g^{-1} , corresponding to 85% and 62% of their initial capacity, respectively. The overpotential is evaluated from the difference between charge potential and discharge potential at the half reversible capacity, noted as $\Delta V(Q/2)$ (Figure 3c).^[33,34] The overpotential of HNS (93 mV) is much lower than that of PNB (152 mV). The electrochemical impedance spectra (EIS) were used to provide further insights (Figure 3d). The Nyquist plots indicate that the charge transfer resistance (R_{ct}) of HNS cathode is 62Ω , much lower than 110Ω for PNB, which is consistent with the overpotential values. Moreover, after ten cycles, the R_{ct} of HNS and PNB increase 17Ω and 70Ω , respectively. These above results demonstrate that the HNS exhibited better structure stability and cyclability than PNB, and suggest that HNS has faster kinetics for Li ion insertion/extraction.^[33–36]

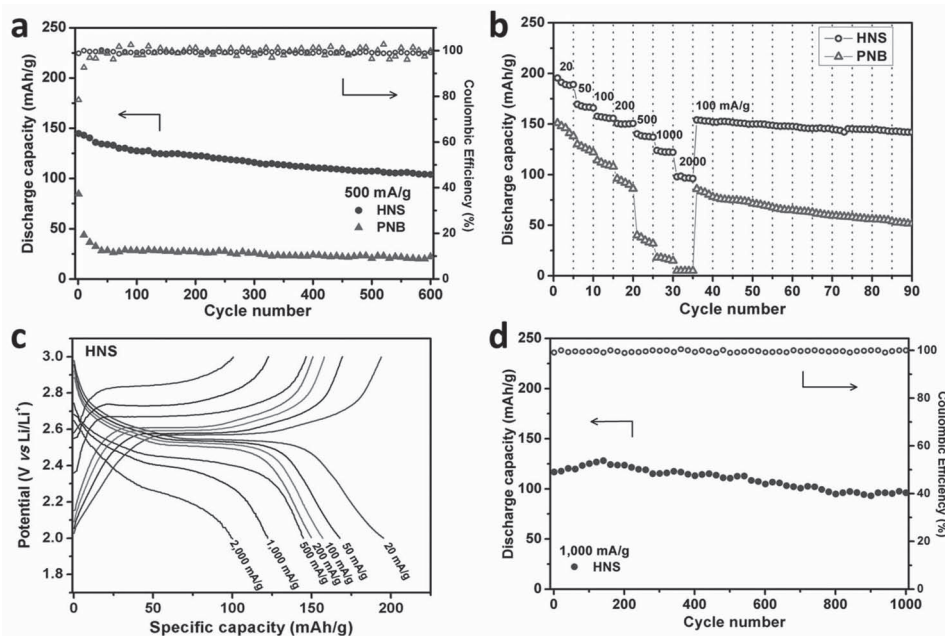


Figure 4. High-rate and long-life performance of HNS cathodes. a) Performance of the HNS and PNB cathodes cycled at 500 mA g^{-1} and the corresponding coulombic efficiency. b,c) Rate performance (b) and initial charge-discharge curves at various current densities from 20 to $2,000 \text{ mA g}^{-1}$, respectively. d) Long-life cycling performance at $1,000 \text{ mA g}^{-1}$.

The performance improvement of the hybrid nanostructure was further tested at higher rates (Figure 4). At 500 mA g^{-1} (Figure 4a), the initial discharge capacity of HNS cathode is 145 mAh g^{-1} , which is about 1.7 times the capacity of PNS (85 mAh g^{-1}). After 600 cycles, the capacity of HNS is 104 mAh g^{-1} , corresponding to 71% of the initial capacity. However, the capacity of PNB quickly decreases to around 25 mAh g^{-1} after 50 cycles. These results directly indicate the great advantage of hybrid nanostructure for high-rate and long-life charge/discharge. To evaluate the advantage of the synergistic effect in the hybrid nanostructure, rate performance at progressively increased current density (ranging from 20 to $2,000 \text{ mA g}^{-1}$) was measured (Figure 4b,c). A discharge capacity of 98 mAh g^{-1} is obtained at $2,000 \text{ mA g}^{-1}$ ($\sim 20^\circ\text{C}$). Even suffering from rapid change of the current density, the electrode exhibits stable capacity at each current. When the current was turned back to 100 mA g^{-1} , about 98.7% of the capacity is recovered and there is no obvious capacity loss after the following 55 cycles. Long-life cycles of HNS cathode at high current density of $1,000 \text{ mA g}^{-1}$ ($\sim 9^\circ\text{C}$) is subsequently shown (Figure 4d). The initial discharge capacity of 117 mAh g^{-1} is achieved. The capacity retention is 90% after 500 cycles and 82% of the initial discharge capacity remain after 1,000 cycles. Meanwhile, the coulombic efficiency stays at $\sim 100\%$ in the overall battery operation.

Traditionally, the specific surface area of electrode materials greatly influences the battery performance. In our case, the cyclability and rate capability of HNS are much better than that of PNB, while the surface area of HNS ($23.2 \text{ m}^2 \text{ g}^{-1}$) is slightly larger than that of PNB ($18.6 \text{ m}^2 \text{ g}^{-1}$). Hence, the significant improvement of the cycling stability and rate performance is mainly attributed to the novel hybrid nanostructure. Firstly, the nanoscrolls and the interconnected voids between hybrid nanostructures as the buffered section could be able to buffer

the volume swelling during lithiation/delithiation, contributing to robust mechanical stability and the excellent cyclability.^[26,27] SEM images show that the nanoscrolls in the HNS after 100 cycles are overall preserved (Figure S8). By the XRD results, there are undetectable gross structure changes of HNS after cycles, while obvious crystallinity decrease are observed in PNB (Figure S9).^[23,35] These results further confirm that HNS is a stable nanostructure for use as an electrode in long-life lithium batteries. Secondly, for PNB, the pure nanobelts stack closely, which may decrease the effective electrolyte-electrode contact area and limit the ion diffusion, corresponding to the large overpotential (152 mV) and R_{ct} (110Ω), which results in the poor cyclability and rate performance. However, for HNS, the interior of nanoscrolls and the interconnected voids offer effective electrolyte-electrode contact area to reduce the ion diffusion pathway, corresponding to the small overpotential (93 mV) and R_{ct} (62Ω). Meanwhile, the synergistic combination of nanoscrolls, nanowire and nanobelts offer stable nanostructure to promptly accommodate the volumetric changes during rapid ion insertion/deinsertion, resulting in its long-life and high-rate performance.

In summary, nanoscroll buffered HNS VO_2 (B) composed of nanobelts and nanowires were synthesized through hydrothermal-driven splitting and self-rolled method. The HNS with buffered section is able to offer facile strain relaxation and shorten the lithium ion diffusion distances. The HNS cathode exhibits long-life performance with capacity retention over 82% after 1,000 cycles at $\sim 9^\circ\text{C}$ ($1,000 \text{ mA g}^{-1}$), and high rate up to $\sim 20^\circ\text{C}$ ($2,000 \text{ mA g}^{-1}$). This unique HNS can be applied to the next-generation high-performance batteries for portable electronics and large-scale energy storage devices. Constructing the nanoscroll buffered hybrid nanostructure described in this paper is a facile and effective method to enhance the electrochemical performance of other electrode materials.

Experimental Section

Synthesis of hybrid nanostructural VO₂ (B) and pure nanobelt VO₂ (B): Inorganic V₂O₅ sols (0.05 M) were prepared through a melt quenching process.^[29] For the synthesis of hybrid nanostructural VO₂ (B), poly(vinyl pyrrolidone) (PVP K30, 17 mg) and poly(ethylene glycol) (PEG 400, 60 μL) were put into V₂O₅ sols (30 mL) under stirring, and the distilled water was added to reach 60 mL. The precursor was stirred for one day and aged for another one day, then transferred to a 100 mL Teflon lined autoclave and kept in an oven at 180 °C for 48 h. The final product was washed with deionized water and pure alcohol several times and then dried at 60 °C in air for 24 h. The synthesis of pure nanobelt VO₂ (B) was similar with that of the hybrid nanostructural VO₂ (B) except for only adding 30 mL PEG.

Materials Characterization: X-ray diffraction (XRD) data of samples were collected with a D8 Advance X-ray diffractometer, using Cu Kα radiation (λ = 1.5418 Å) in a 2θ range from 10° to 80° at room temperature. The microstructures were observed by Field-emission scanning electron microscopy (FESEM) (Hitachi S-4800, 10 kV), and transmission electron microscopy (TEM) and high-resolution transmission electron microscopy (HRTEM), (JEM-2100F). Brunauer-Emmerr-Teller surface area was measured using ASAP 3020M instrument by adsorption of nitrogen at -209 °C.

Electrochemical measurements: The electrochemical properties were characterized in coin cells with lithium metal foil as the anode. The cathode electrodes were composed of 70% active material, 20% acetylene black and 10% poly(tetrafluoroethylene) (PTFE) binder. A solution (1 M) of LiPF₆ in EC/DEC (1:1 vol/vol) was used as the electrolyte. The cells were assembled in an argon-filled glove-box. Galvanostatic charge/discharge measurement was performed by a multichannel battery testing system (LAND CT2001A), cycling voltammetry (CV) and electrochemical impedance spectroscopy (EIS) were tested with an Autolab Potentiostat Galvanostat. All the measurements were carried out at room temperature.

Supporting Information

Supporting Information is available from the Wiley Online Library or from the author.

Acknowledgements

This work was supported by the National Basic Research Program of China (2013CB934103, 2012CB933003), National Natural Science Foundation of China (51072153, 51272197), the International Science & Technology Cooperation Program of China (2013DFA50840), the Program for New Century Excellent Talents in University (NCET-10-0661) and the Fundamental Research Funds for the Central Universities (2012-II-001). Thanks to Prof. Dongyuan Zhao of Fudan University for his kind supervision, stimulating discussion and strong support. Thanks to Prof. C.M. Lieber of Harvard University and Dr. Jun Liu of Pacific Northwest National Laboratory for strong support and stimulating discussion.

Received: December 18, 2012

Revised: January 30, 2013

Published online: March 21, 2013

- [1] B. Kang, G. Ceder, *Nature* **2009**, 458, 190.
 [2] B. Dunn, H. Kamath, J. M. Tarascon, *Science* **2011**, 334, 928.
 [3] a) H. Wu, G. Chan, J. W. Choi, I. Ryu, Y. Yao, M. T. McDowell, S. W. Lee, A. Jackson, Y. Yang, L. Hu, *Nat. Nanotech.* **2012**, 7, 310; b) H. Zhang, X. Yu, P. V. Braun, *Nat. Nanotech.* **2011**, 6, 277.
 [4] a) H. Liu, D. Su, R. Zhou, B. Sun, G. Wang, S. Z. Qiao, *Adv. Energy Mater.* **2012**, 2, 970; b) H. Liu, X. Du, X. Xing, G. Wang, S. Z. Qiao, *Chem. Commun.* **2012**, 48, 865; c) H. Liu, D. Su, G. Wang, S. Z. Qiao, *J. Mater. Chem.* **2012**, 22, 17437.
 [5] S. R. Gowda, A. Leela Mohana Reddy, X. Zhan, H. R. Jafry, P. M. Ajayan, *Nano Lett.* **2012**, 12, 1198.
 [6] M. S. Whittingham, *Chem. Rev.* **2004**, 104, 4271.
 [7] J. Yan, A. Sumboja, E. Khoo, P. S. Lee, *Adv. Mater.* **2011**, 23, 746.
 [8] T. Zhai, H. Liu, H. Li, X. Fang, M. Liao, L. Li, H. Zhou, Y. Koide, Y. Bando, D. Golberg, *Adv. Mater.* **2010**, 22, 2547.
 [9] A. Pan, J.-G. Zhang, Z. Nie, G. Cao, B. W. Arey, G. Li, S. Liang, J. Liu, *J. Mater. Chem.* **2010**, 20, 9193.
 [10] N. A. Chernova, M. Roppolo, A. C. Dillon, M. S. Whittingham, *J. Mater. Chem.* **2009**, 19, 2526.
 [11] W. Li, J. Dahn, D. Wainwright, *Science* **1994**, 264, 1115.
 [12] a) J. Liu, Q. Li, T. Wang, D. Yu, Y. Li, *Angew. Chem. Int. Ed.* **2004**, 43, 5048; b) J. Huang, X. Wang, J. Liu, X. Sun, L. Wang, X. He, *Int. J. Electrochem. Sci.* **2011**, 6, 1709.
 [13] E. Baudrin, G. Sudant, D. Larcher, B. Dunn, J. M. Tarascon, *Chem. Mater.* **2006**, 18, 4369.
 [14] J.-H. Son, J. Wei, D. Cobden, G. Cao, Y. Xia, *Chem. Mater.* **2010**, 22, 3043.
 [15] W. Chen, L. Mai, Y. Qi, Y. Dai, *J. Phys. Chem. Solids* **2006**, 67, 896.
 [16] H. Liu, Y. Wang, K. Wang, E. Hosono, H. Zhou, *J. Mater. Chem.* **2009**, 19, 2835.
 [17] C. V. Subba Reddy, E. H. Walker, S. A. Wicker, Q. L. Williams, R. R. Kalluru, *Curr. Appl. Phys.* **2009**, 9, 1195.
 [18] G. Armstrong, J. Canales, A. R. Armstrong, P. G. Bruce, *J. Power Sources* **2008**, 178, 723.
 [19] Q. Zhao, L. Jiao, W. Peng, H. Gao, J. Yang, Q. Wang, H. Du, L. Li, Z. Qi, Y. Si, Y. Wang, H. Yuan, *J. Power Sources* **2012**, 199, 350.
 [20] L. Q. Mai, F. Yang, Y. L. Zhao, X. Xu, L. Xu, Y. Z. Luo, *Nature Commun.* **2011**, 2, 381.
 [21] J. Liu, J. Jiang, C. Cheng, H. Li, J. Zhang, H. Gong, H. J. Fan, *Adv. Mater.* **2011**, 23, 2076.
 [22] Y. Zhao, L. Xu, L. Mai, C. Han, Q. An, X. Xu, X. Liu, Q. Zhang, *Proc. Natl. Acad. Sci. USA* **2012**, 109, 19569.
 [23] L. Mai, L. Xu, C. Han, X. Xu, Y. Luo, S. Zhao, Y. Zhao, *Nano Lett.* **2010**, 10, 4750.
 [24] J. Liu, J. S. Chen, X. Wei, X. W. Lou, X.-W. Liu, *Adv. Mater.* **2011**, 23, 998.
 [25] A. Kumar, A. L. M. Reddy, A. Mukherjee, M. Dubey, X. Zhan, N. Singh, L. Ci, W. E. Billups, J. Nagurny, G. Mital, *ACS Nano* **2011**, 5, 4345.
 [26] A. K. Schaper, M. S. Wang, Z. Xu, Y. Bando, D. Golberg, *Nano Lett.* **2011**, 11, 3295.
 [27] S. F. Braga, V. R. Coluci, S. B. Legoas, R. Giro, D. S. Galvão, R. H. Baughman, *Nano Lett.* **2004**, 4, 881.
 [28] F. Zeng, Y. Kuang, G. Liu, R. Liu, Z. Huang, C. Fu, H. Zhou, *Nanoscale* **2012**, 4, 3997.
 [29] Y. Xiong, I. Washio, J. Chen, H. Cai, Z. Y. Li, Y. Xia, *Langmuir* **2006**, 22, 8563.
 [30] L. Kong, Z. Liu, M. Shao, Q. Xie, W. Yu, Y. Qian, *J. Solid State Chem.* **2004**, 177, 690.
 [31] A.-M. Cao, J.-S. Hu, H.-P. Liang, L.-J. Wan, *Angew. Chem. Int. Ed.* **2005**, 44, 4391.
 [32] a) L. Shen, N. Bao, K. Yanagisawa, K. Domen, C. A. Grimes, A. Gupta, *The J. Phys. Chem. C* **2007**, 111, 7280; b) J. M. Song, Y. Z. Lin, H. B. Yao, F. J. Fan, X. G. Li, S. H. Yu, *ACS Nano* **2009**, 3, 653.
 [33] L. Q. Mai, B. Hu, W. Chen, Y. Y. Qi, C. S. Lao, R. S. Yang, Y. Dai, Z. L. Wang, *Adv. Mater.* **2007**, 19, 3712.
 [34] L. Hu, F. La Mantia, H. Wu, X. Xie, J. McDonough, M. Pasta, Y. Cui, *Adv. Energy Mater.* **2011**, 1, 1012.
 [35] Y. Wu, Z. Wen, J. Li, *Adv. Mater.* **2011**, 23, 1126.
 [36] X. Xu, Y. Z. Luo, L. Q. Mai, Y. L. Zhao, Q. Y. An, L. Xu, F. Hu, L. Zhang, Q. J. Zhang, *NPG Asia Mater.* **2012**, 4, e20.